High-Resolution Coastal Winds from the NOAA Near Real-Time ASCAT Processor

Seubson Soisuvarn, Zorana Jelenak, Paul S. Chang, Qi Zhu, and Casey G. Shoup

Abstract—The NOAA near real-time operational ASCAT ocean surface wind vectors are produced at 12.5 and 25 km swath grid resolutions. To avoid land contamination due to the relatively large footprint size, the wind data in the inner most coastal regions (~15 - 25 km from the coast) are excluded from the final product. To obtain more retrievals in the coastal regions we utilize measurements containing up to 50% land contribution ratio and employ a combination of the enhanced resolution processing technique and a coastal normalized radar cross section correction method to achieve accurate wind retrievals to within ~1.0 - 2.5 km of the coast. The backscatter correction is implemented for each ASCAT coastal zone measurement. The mean and standard deviation of the land contribution for each measurement is determined, and then the land backscatter contribution is subtracted out from the actual measurement through an iteration method to estimate the ocean-only signal. An ocean calibration of the enhanced resolution backscatter was implemented before the wind retrieval step to improve the accuracy. Finally, a land contribution ratio ranking is implemented after the wind retrieval to further remove the remaining land contamination residuals. Additional quality control is also developed. The high-resolution coastal winds from ASCAT are validated against a variety of other independent wind measurements. The results are then presented and discussed.

Index Terms—ASCAT, Scatterometer, High-Resolution, Coastal Winds.

I. INTRODUCTION

THE coastal sea surface wind field information is important for a number of applications, such as marine weather forecasting, coastal management, fisheries management, ice motion, recreational boating, food and oil production, and energy harvesting. The oceanic vertical motion induced by winds and currents is also important to biology and biogeochemistry within the ocean column. The Advanced SCATterometer (ASCAT) is capable of providing this important wind information over the global oceans. The ASCAT sensors were developed by the European Space Agency (ESA) and are operated by the European organization for the exploitation of METeorological SATellites (EUMETSAT) [1]. The first ASCAT was launched on-board the MetOp-A satellite, so called the ASCAT-A, on 19 October 2006 and was decommissioned on 15 November 2021. The follow-on ASCAT-B and -C were launched on MetOp-B and MetOp-C on 17 September 2012 and 7 November 2018, respectively and they are still operational at the time of this writing. ASCAT, a microwave radar instrument, operates at a frequency of 5.255 GHz (C-band). It transmits and receives radar pulses using two sets of three vertically polarized fixed fan-beam antennas. The return radar backscatter power is used to calculate the normalized radar cross-section (NRCS) or sigma0 (σ^0) measurements used in the wind retrieval algorithm. The antennas illuminate fan beams looking ±45° forward (fore beams), ±90° sideway (mid beams) and ±135° backward (aft beams) with respect to the satellite's flight direction to create a measurement swath of approximately 550-km on each side for the satellite ground track with a 700 km gap between the two swaths. The illuminated antenna footprint of the fore and aft beams span incidence angles between 37°-64°; while the mid beam footprint spans incidence angles between 27°-52° with the shape and size of the spatial response function (SRF) of the individual NRCS samples as defined in [2] [3]. As the satellite moves forward, a triplet of sigma0 measurement within a wind vector cell (WVC) from the fore, mid and aft beams are used to retrieve the ocean surface wind vector through an empirically derived Geophysical Model Function (GMF) [4] [5] [6] [7]. The wind retrievals are derived for each WVC (typically at 12.5 km or 25 km sampling) along and across the swaths.

NOAA has operationally produced near real-time global ASCAT ocean surface wind vector products at 12.5 km and 25 km swath grid resolutions [6] since 2007. While extremely valuable to NOAA's user community [8], the coverage of these data products are quite limited in the coastal area because the relatively coarse spatial resolution required a conservative land mask to avoid land contamination in the coastal zone grid cells. This results in no wind data within ~15 - 25 km of the coast. To enhance usability of ASCAT data within inner most coastal zones we have developed a coastal ASCAT wind data product using a combination of a high-resolution processing technique [9] [10] [11] [12] [13] and an NRCS correction approach. This

The authors are with the Center for Satellite Applications and Research, National Environmental Satellite, Data, and Information Service, National Oceanic and Atmospheric Administration, 5830 University Research Ct. College Park, MD 20740 USA (e-mail: seubson.soisuvarn@noaa.gov)

Color versions of one or more of the figures in this article are available online at http://ieeexplore.ieee.org

allowed us to produce winds within ~1 – 2.5 km of the coast [14] [15]. The high-resolution data processing has been implemented in a near real-time environment similar to the processing for the lower resolution products. However, the extensive computational requirements of the high-resolution processor, the near real-time high-resolution data is currently limited to the Alaska coastal region presented here: https://manati.star.nesdis.noaa.gov/datasets/AlaskaASCATCoastal.php. To achieve acceptable accuracy for operational applications, an ocean calibration of the enhanced resolution backscatter was necessary and implemented before the wind retrieval step similar as was done for the low-resolution products [16] [17]. This paper is organized in the following sections. In Section II, a brief background of the ASCAT high-resolution processing technique is provided. Section III details key improvements in the land contamination removal using a sigma0 correction approach. Section IV shows how the high-resolution sigma0 calibration was done. In Section V, the enhanced resolution coastal wind results are demonstrated and a quality control flag for the high-resolution winds is discussed. In Section VI, the validation results against a variety of other independent wind measurements are presented. Finally, the paper is concluded in Section VII.

II. RESOLUTION ENHANCEMENT BACKGROUND

The individual sigma0 measurements from each ASCAT antenna beam are contained in the Level 1B full resolution SZF data product [3]. It has been shown in [13] [18] that the sigma0 resolution can be significantly improved by implementing the image reconstruction and resolution enhancement algorithm processing techniques. In this paper, we make use of a resolution enhancement technique known as the weighted AVErage (AVE) algorithm [13] developed by the Brigham Young University (BYU) to process ASCAT L1B sigma0's into the ultra-high-resolution (UHR) sigma0 and ultimately the UHR coastal wind data.

A. ASCAT Sigma0 Measurement

ASCAT samples the earth surface using 6 fan-beam antennas (3 beams on each side of the ground track). The smallest element of the measurement is recorded in the L1B "full-resolution" SZF data product. There are 192 or 256 sigma0 measurement "cells" or "slices" along the beams depending on the L1B data version. Each sigma0 is measured at a different incidence angle along the beams, where the measurement geometry footprint is varying slightly with changing incidence angle. For an ith sample sigma0, neglecting the measurement noise, the sigma0 measurement σ^0_i can be expressed as a weighted integration of the surface sigma0 $\sigma^0(x,y)$ and the measurement Spatial Response Function (SRF) $h_i(x,y)$ as [2]

$$\sigma_i^0 = \frac{\iint \sigma^0(x,y)\, h_i(x,y)dxdy}{\iint h_i(x,y)dxdy}$$

where the x and y are spatial variables in the x and y dimension. The SRF is essentially the antenna gain pattern projection on the surface. Detailed information about the ASCAT SRF can be found in [2]. Within the enhanced resolution processor, the high-resolution sigma0 is derived by the recovery of the $\sigma^0(x,y)$ given a set of σ^0_i and $h_i(x,y)$ measurements.

B. Enhanced Resolution Algorithm

The first step of the resolution enhancement algorithm is to populate a fine resolution grid with the earth surface $\sigma^0(x,y)$ from which an ultra-high-resolution (UHR) sigma0 is derived from each grid cell or pixel (grid spacing). From (1), the measured sigma0 σ^0_i can be expressed in a discrete form as in [13]

$$\sigma_i^0 = \sum_{j=1}^{n} h_{ij}\sigma_{ij}^0$$

where h_{ij} and σ^0_{ij} is the weighted SRF value of $h_i(x,y)$ and the value of $\sigma^0(x,y)$ respectively from the ith measurement and the jth pixel. The σ^0_i is a weighted summation of the total number of pixels n bounded by the SRF measurement contour [13] [2]. By taking advantage of the nonuniformity in the SRF and overlapping measurements, a high spatial resolution sigma0 can be extracted. The simplest inversion algorithm to estimate the σ^0_{ij} is the weighted AVErage (AVE) algorithm. Unlike the other enhanced resolution algorithms where multi-pass observations are required, the AVE algorithm utilizes single pass snapshot from all three beams where the temporal and azimuthal information sensitive to the change in the surface condition is preserved. The measurement geometry information such as incidence angle and azimuth angle associate with each pixel are carried along so that they can be used in the wind retrieval algorithm. The enhanced resolution technique was successfully utilized to produce high resolution wind fields within tropical cyclones [18] and it has also been shown that it can be used for wind retrievals in coastal waters as well as for sea ice observations [18]. The AVE sigma0 (σ^0_{ave}) is basically a weighted average of all overlapping sigma0 measurement slices. The algorithm requires a number of σ^0_i measurement samples for each ASCAT beam to meet the Nyquist sampling criteria [10]. Our coastal processor, utilized the AVE algorithm and the software developed by the Brigham Young University (BYU) to calculate $\sigma^0_{ave,j}$ for each ASCAT beam. For each ASCAT beam, the AVE algorithm can be expressed as

$$\sigma_{ave,j}^0 = \frac{\sum_i \sigma_i^0 h_{ij}}{\sum_i h_{ij}}$$

As the satellite moves forward, a swath of σ^0_{ave} pixels are generated for each ASCAT fore, mid and aft beams. The UHR pixels were populated onto a latitude and longitude grid and the corresponding h_{ij} on that grid was used to calculate $\sigma^0_{ave,j}$ in (3). In this paper, we selected the finest grid spacing possible in the BYU software that still satisfied the Nyquist sampling criteria, resulting in a grid spacing of approximately 1.5 km, where the effective spatial resolution is coarser than 1.5 km [13]. An example of the UHR sigma0 pixels σ^0_{ave} for the aft-left ASCAT measurement swath are depicted in Fig. 1 In this example sigma0 observations over land, land-sea boundary and open ocean is present.
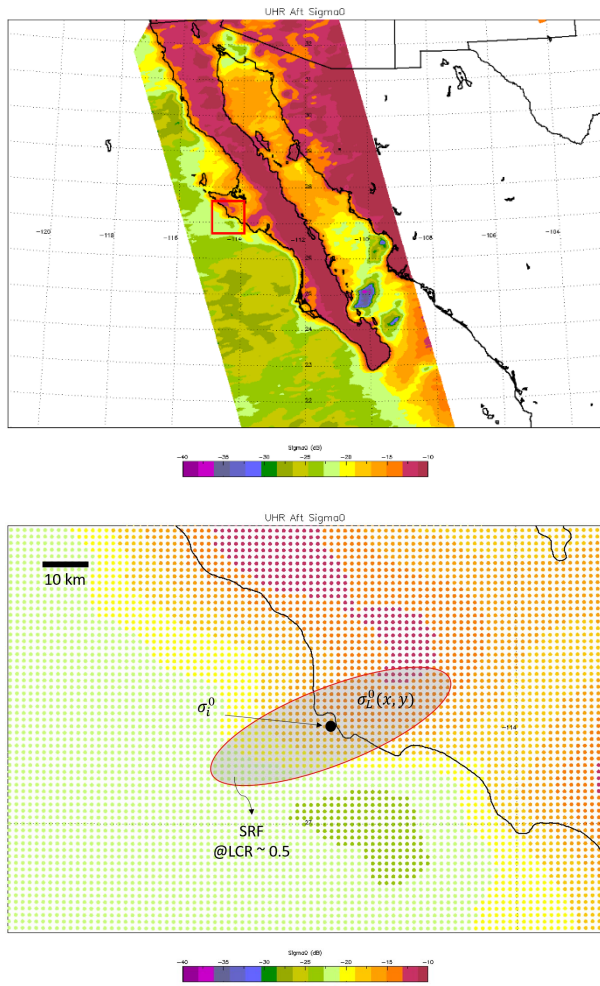

Fig. 1. Example of the Ultra High-Resolution (UHR) sigma0 using the AVE algorithm processing technique in the Gulf of California (top). The close-up of the UHR pixels in the square red box is shown in the bottom image. The ellipse represents the -3dB contour of the SRF with approximately 50% land observations within.

III. LAND CONTAMINATION CORRECTION

As the satellite crosses over land-sea boundary, we get sigma0 slice measurements containing different percentages of land contributions to the measured signal. Therefore, σ^0_i contributing to the σ^0_{ave} have different levels of land contamination. Typically, the land signal is much stronger than the ocean signal. As seen in Fig. 1, the coastal outline is depicted by orange and yellow colors indicating that the land signal is "leaking" into the ocean. If this is not treated properly, the wind speed estimates resulting from land contaminated sigma0 in the coastal regions can be extremely high. To address this problem, we have developed a land contamination correction method. This correction has to be implemented in the sigma0 slice measurement (σ^0_i) level. From (1), the sigma0 can be rewritten as a summation of the land-only sigma0 and ocean-only sigma0 contributions as

$$\sigma^0_i = \sigma^0_{Land} + \sigma^0_{Ocean}$$

where the land-only sigma0 can be further expanded into a discrete form as

$$\sigma^0_{Land} = \frac{\sum \sigma^0_L(x,y) \cdot G_L(x,y)}{\sum G_{Total}(x,y)}$$

and

$$\sigma^0_{Land} = \frac{\sum \sigma^0_L(x,y) \cdot G_L(x,y)}{\sum G_L(x,y)} \cdot \frac{\sum G_L(x,y)}{\sum G_{Total}(x,y)}$$

where the $\sigma^0_L(x,y)$ is the surface sigma0 over land, the $G_L(x,y)$ is the gain response portion over land and the $G_{Total}(x,y)$ is the total gain response. Let us define the first term in (6) as the weighted average land contribution term $\sigma^0_{L,ave}$

$$\sigma^0_{L,ave} = \frac{\sum \sigma^0_L(x,y) \cdot G_L(x,y)}{\sum G_L(x,y)}$$

and the second term in (6) is defined as the land contribution ratio (LCR) [13]

$$LCR = \frac{\sum G_L(x,y)}{\sum G_{Total}(x,y)}$$

In the open ocean, where there is no land contamination, the LCR is 0. As the measurement get closer to the coast, the LCR is always > 0 and is 1 when the entire measurement slice is over land. By keeping track of the LCR for each slice, it is possible to reject the measurement with too high of a land contamination based on a pre-defined threshold. This approach has been demonstrated by [18] [19]. In previous work, the LCR rejection threshold was set very low; e.g. LCR ≤ 0.01 or 1%. This resulted in many coastal sigma0 slices being rejected; leaving

again the most inner coastal waters still void of any wind retrievals. In our approach to maximize the inner coastal zone coverage, we use an LCR threshold up to 0.5 or 50 % land contamination. In order to utilize slices with higher land contamination, we need to estimate land-only sigma0 and subtract it from the overall measurement. Using (6)-(8), land-only sigma0 can be expressed as
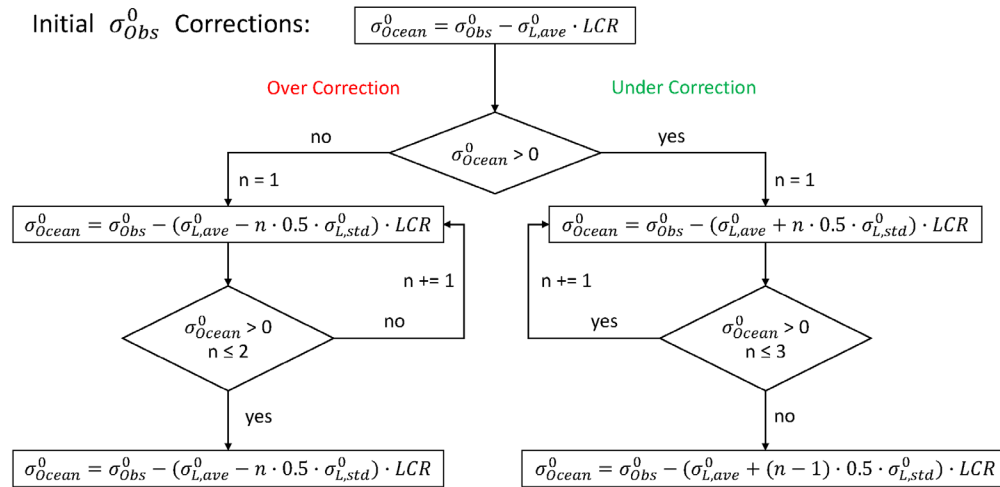

Fig. 2. A diagram showing the sigma0 land contamination correction process.

$$\sigma^0_{Land} = \sigma^0_{L,ave} \cdot LCR$$

Utilizing the SRF values and a fine resolution land mask the LCR calculation is straightforward using (8). The land mask we utilize for this calculation has a resolution of $1/100°$ in both North-South and West-East dimensions. To estimate the $\sigma^0_{L,ave}$, the $\sigma^0_{ave,j}$ was initially computed for both land and ocean pixels, as depicted in Fig. 1. Subsequently, by utilizing only the land segment of $\sigma^0_L(x,y)$, the $\sigma^0_{L,ave}$ can be calculated through (7). This land sigma0 area is also indicated in Fig. 1. The $G_L(x,y)$ is also pre-determined at the same (x,y) pixels. Using (4) and (9), initially we calculate ocean sigma0 by subtracting estimated land sigma0 portion from the original measurement:

$$\sigma^0_{Ocean} = \sigma^0_i - \sigma^0_{L,ave} \cdot LCR$$

Depending on the land geographical features and measurement orientation, the $\sigma^0_{L,ave}$ can vary greatly, and therefore, the land corrected sigma0 in (10) is sometimes under-corrected or over-corrected. To account for terrain differences, we introduce another term: the weighted land standard deviation $\sigma^0_{L,std}$ defined as

$$\sigma^0_{L,std} = \left(\frac{\sum \left[\left(\sigma^0_L(x,y) - \sigma^0_{L,ave} \right) \cdot G_L(x,y) \right]^2}{\sum G_L(x,y)} \right)^{0.5}$$

The $\sigma^0_{L,std}$ is a measure for the land sigma0 variability within the measurement slice. The flow chart of the land correction algorithm that makes use of the $\sigma^0_{L,std}$ is shown Fig. 2. The final land correction for each sigma0 measurement is determined through an iterative process, where n represents the iteration number.

The iterations are carried out until the corrected sigma0 produces non-negative value or until it reaches a maximum of $n = 3$ iterations. Finally, the corrected sigma0 σ^0_{Ocean} is substituted for σ^0_i in (3) and used to estimate minimally contaminated coastal UHR sigma0 as in (12).

$$\sigma^0_{ave,j} = \frac{\sum_i \sigma^0_{Ocean} h_{ij}}{\sum_i h_{ij}}$$

An example of the UHR sigma0's calculated by allowing the measurement slices with LCR ≤ 0.5, before and after land contamination corrections as described above, are demonstrated in Fig. 3.While the majority of land contamination is corrected with this procedure, there are still some instances where land contamination remains an issue. To help eliminate those measurements within our processing algorithm we calculate and keep track of the UHR sigma0 utilizing five different LCR thresholds between 0.1 ≤ LCR ≤ 0.5 in steps of 0.1. They are all ranked based on contamination probability defined by LCR level. The best ranked LCR are later used to select an LCR threshold for the final estimated wind.
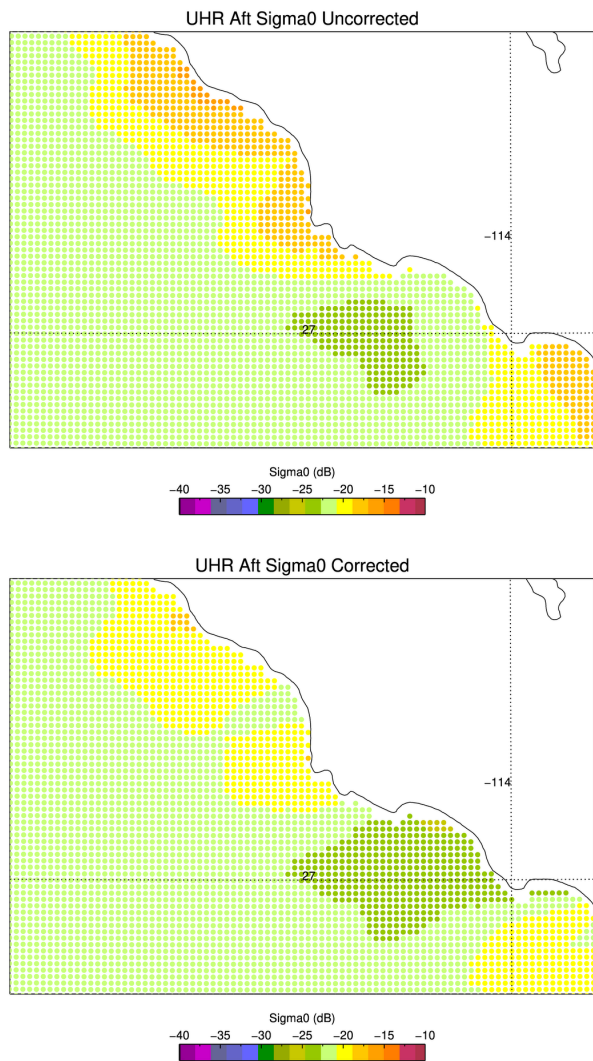
IV. OCEAN CALIBRATION

Fig. 3. A comparison of the UHR sigma0 using 50% LCR threshold before land contamination correction (top) and after land contamination correction (bottom).

The sigma0 calibration is needed to achieve acceptable wind retrieval accuracy for operational utilization. This calibration is required in order to provide a mean correction for large-scale weather variability and to correct for instrument measurement variation of the scatterometer system [16] [17]. In the NOAA near real-time 12.5 km and 25 km products, the sigma0 calibration is applied as a function of node number across the swath for each sigma0 beam prior to wind retrieval [16] [17]. However, for the UHR sigma0, the calibration is applied as a function of incidence angle. Since the calibration values are obtained by fitting the measured sigma0 to the simulated sigma0 determined from the GMF using the same measurement geometry and collocated NWP model wind speeds and directions (commonly referred to as an ocean calibration), the calibration values are dependent on the GMF version utilized and the ASCAT platform. The CMOD5.H GMF [6] is utilized in the NOAA ASCAT operational products so for consistency the CMOD5.H GMF is also used to calibrate the UHR sigma0. The bin average of the sigma0 residuals between the measurement and the GMF for each fore, mid and aft beam are calculated, in dB, as a function of incidence angles and presented in Fig 4. The residuals are fitted with a third-order polynomial. The coefficients are determined separately for ASCAT-A, ASCAT-B and ASCAT-C. The calibration functions for each ASCAT is shown in Fig. 4. The calibration regression as a function of incidence angle is represented by the dash lines and the coefficients of the third-order polynomial function are presented in Table I. The shape of the calibration correction among ASCATs is similar but the offsets are slightly different. Prior to the UHR wind retrieval processing, the calibration correction is applied to each UHR sigma0 beam and its corresponding incidence angle. The calibrated UHR sigma0 can be expressed as

$$\sigma^0_{Cal,j} = \sigma^0_{ave,j} + \Delta\sigma^0(\theta_j)$$

where the $\Delta\sigma^0(\theta_j)$ is the calibration value for j^{th} pixel at θ_j incidence angle.
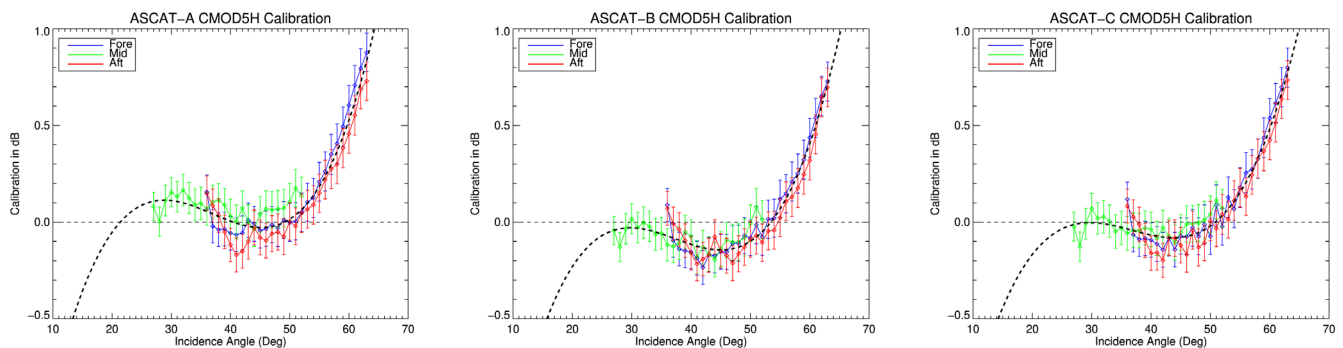

Fig. 4. A bin average and calibration regression function as a function of incidence angle for (a) ASCAT-A, (b) ASCAT-C and (c) ASCAT-C. The error bars represent the sigma0 standard deviation scaled by a factor of 20.

TABLE I
CALIBRATION REGRESSION COEFFICIENTS

	ASCAT-A	ASCAT-B	ASCAT-C
a_1	0.25	0.26	0.22
a_3	6.43e-5	6.47e-5	5.70e-5

V. HIGH-RESOLUTION COASTAL WIND RETRIEVALS

The processing software for ASCAT high resolution coastal wind retrievals was developed by BYU. An overview of the processor is depicted in Fig. 5. The modifications that we implemented in the processor and discussed in previous sections are indicated by the green rectangular boxes in Fig. 5. The NOAA high-resolution coastal wind processing was setup to run in the NOAA/NESDIS/STAR Ocean Winds Team near real-time environment. The processor requires inputs from the near real-time ASCAT full resolution L1B SZF sigma0 file and the ASCAT 12.5 km winds retrievals. The ASCAT 12.5 km retrievals are used in the ambiguity removal step where high-resolution wind directions are estimated. The previous sections described the steps to prepare and calibrate the UHR sigma0 before the wind retrieval step. The wind retrieval algorithm is based on a Maximum Likelihood Estimator (MLE) approach [20], [21], [22]. In this approach, the measured sigma0 from fore, mid and aft beams are compared to the simulated sigma0 through the GMF giving trial wind speeds and wind directions. The wind speeds and directions that produce local minima of the objective function, defined as the sum difference between measured and modeled sigma0's, are determined as the most likely wind solutions. Due to the periodic nature of the GMF, there are typically up to 4 possible solutions, which are often referred to as the wind ambiguities. The ambiguities are ranked according to the residuals or MLEs values, where the smallest MLE is assigned the 1st rank as the most likely solution, the 2nd rank as the second most likely and so on. For the consistency with the 12.5 km product, the UHR wind directional ambiguities are compared to the prior derived 12.5 km wind direction. The ambiguities that minimize that angle between the UHR and collocated 12.5 km wind direction are selected as the unique or chosen wind solution.

The near real-time UHR coastal wind processor was set up to produce wind products from all three ASCAT instruments. In order to maximize the number of pixels in the coastal zone, we have taken an aggressive approach by setting the LCR threshold to 0.5. However, to ensure wind retrievals are obtained from least contaminated measurements we calculate UHR sigma0's for all LCR's between 0.1 and 0.5 at 0.1 steps as noted in the previous section. The UHR wind retrievals are then ranked according to the LCR threshold used, where the higher rank is assigned to the wind retrieval from the smaller LCR threshold. The final coastal wind is then selected from the wind retrievals with the highest rank. The majority of the pixels furthest away

from the coast are wind retrieval from the 0.1 LCR threshold. As we get closer to the coast and 0.1 LCR pixels became unavailable, the wind pixels are then selected from the next highest rank wind solutions from 0.2 – 0.5 LCR threshold accordingly. An example of the NOAA processed coastal UHR ASCAT wind speed is shown in Fig. 6. The overlaying wind direction is the collocated 12.5 km wind which stops ~15 km from the coast. The 12.5 km product also has a narrower swath due to a more limited incidence angle range used in the wind retrievals. One advantage of the UHR sigma0 processing is a full use of all the available sigma0 samples in the Level 1B full resolution data, this results in ~75km swath extension with respect to the 12.5km product. The corresponding histogram of the coastal wind LCR rank selection within ~15 km of the coast from Fig. 6 is shown in Fig. 7.
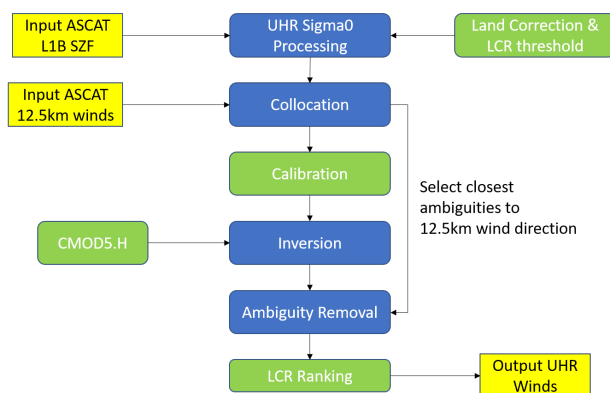

Fig. 5. An overall diagram of the high-resolution coastal wind retrieval processing.

The Fig. 6(a) shows the UHR coastal wind retrievals without using the land contamination correction sigma0 explained in Section III. Erroneous high winds highlighting the shape of the coastline are depicted especially along the coast of the Baja California Sur. The winds within Gulf of California are more affected on the east side of the Baja California Sur than on the west coast of Mexico. In Fig. 6(b), we show the final UHR coastal wind. While all pixels as in Fig 6a are preserved, clearly land contamination is dramatically decreased relative to retrievals from Fig 6(a). A zoomed in version of the same retrievals from Fig 6, within three different areas, around Islands of Angel de la Guarda and Tiburon, Cedros Island and Gulf of Tortugas and Carmen Island are shown in Fig. 8 (a), (b) and (c) respectively. Corresponding 12.5 km retrievals are depicted in top row to demonstrate the increased coverage of the UHR coastal wind product.

Before the coastal wind performance could be properly assessed, a quality control had to be developed to flag any corrupted wind retrievals due to rain impact, land and ice contamination.

GOC, ASCAT−B Ascending, 20220203, 04:16 UTC, UHR Wind Speed

Wind Speed (knot)

0   5   10 15 20 25 30 35 40 45 50

GOC, ASCAT−B Ascending, 20220203, 04:16 UTC, UHR Wind Speed

Wind Speed (knot)

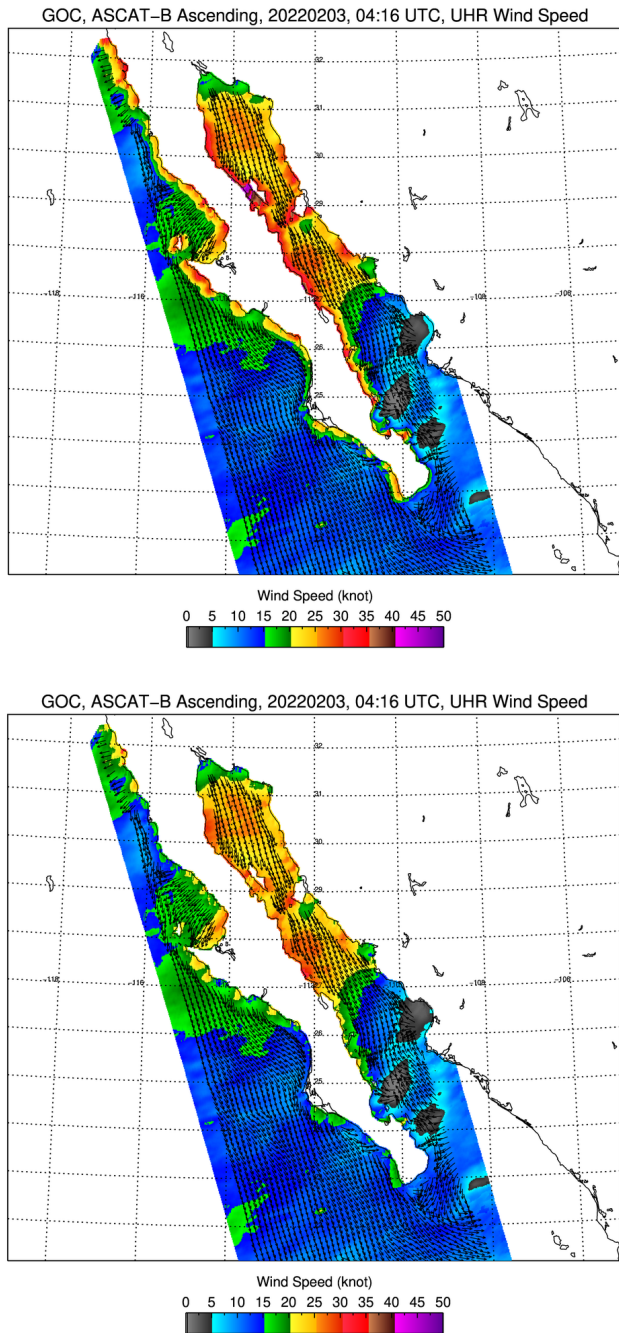0   5   10 15 20 25 30 35 40 45 50

Fig. 6. Example of high-resolution coastal wind in the Gulf of California. (a) before and (b) after land contamination correction. The overlaying arrows represent the 12.5 km wind direction which stops ~15 km from the coast. The 12.5 km product has a narrower swath due to more limited incidence angle range used than with the UHR product.

A. Quality Control

As discussed above, the wind retrieval is based on the Maximum Likelihood Estimator (MLE), and thus, the residual

of the difference between the measurements and the GMF is available for each pixel *j*. The main sources of error in the UHR wind retrievals are from land, ice and rain contaminated measurements. The quality control algorithm for rain and land contamination assumes the MLE residual for a retrieved wind speed will increase for impacted measurements. Therefore, a quality flag can be designed by thresholding the MLE residual defined as:
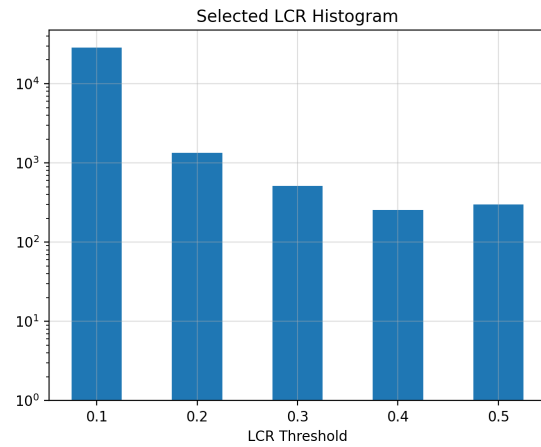

Fig. 7. A histogram of LCR threshold selected as highest ranked (least land contaminated) coastal wind vector.

$$MMLLMM_{TT} = \frac{\sum_{ll=1}^{3}(MMLLMM_{jj,ll})^2}{WWWW} \qquad (14)$$

where $MLE_{j,l}$ is the residual error between the measurements *l* = 1-3 from the fore, mid and aft beams and the model sigma0 at pixel *j*, and *WS* is the retrieved high-resolution wind speed. The numerator of (14) is proportional to the MLE values calculated during the wind retrievals, which can then be used in the numerator. An optimum value of the MLE_r threshold to flag the rain impacted wind retrievals was determined to be when $MLE_r \geq 22$. Fig 9(a) shows an example of high-resolution Hurricane Ida wind speeds that are flagged as rain shown by the black dots. Fig 9(b) shows the corresponding MLE_r. The MLE_r is also used as a land contamination flag when the retrieval was within 30 km of the coast.

The ice contamination flag was first initialized by a coarse ice flag from the GDAS ice mask. A normalized sigma0 for each initially flagged ASCAT beam was then calculated by removing the incidence angle dependence [23]. Finally, the three beams were averaged to get the ice sigma0, σ^0_{ice}. The optimum value of σ^0_{ice} is set to be $\sigma^0_{ice} > -14.5$ dB. If σ^0_{ice} was below this threshold the points initially flagged as ice were unflagged.

1
2
3
4
5
6
7
8
9
10
11
12
13
14
15
16
17
18
19
20
21
22
23
24
25
26
27
28
29
30
31
32
33
34
35
36
37
38
39
40
41
42
43
44
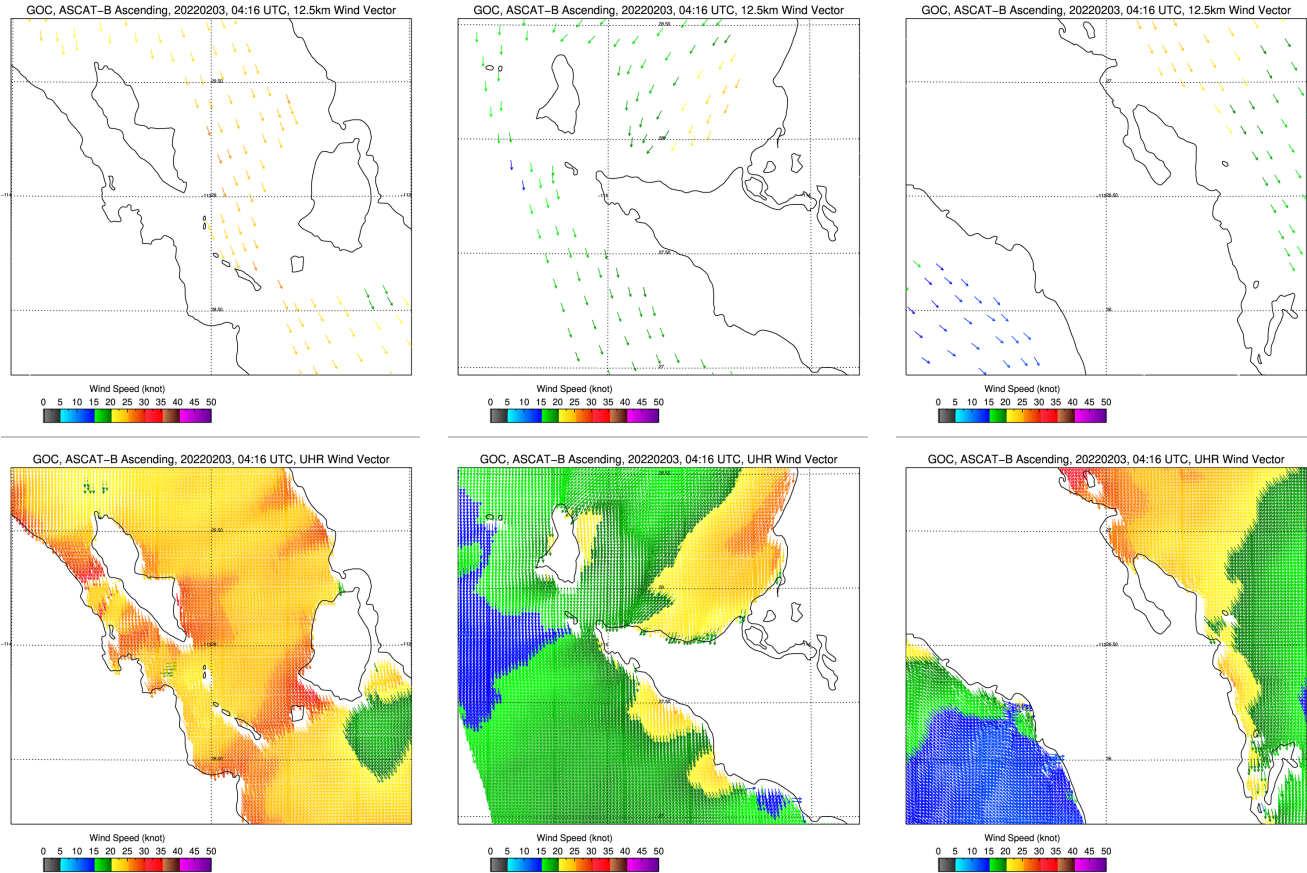45
46
47
48
49
50
51
52
53
54
55
56
57
58
59
60

Fig. 8. Close-up ASCAT wind vectors (the arrows represent the direction and the colors represent the magnitude) from selected coastal area from Fig. 6: standard 12.5 km winds (top row), high-res coastal winds (bottom row).
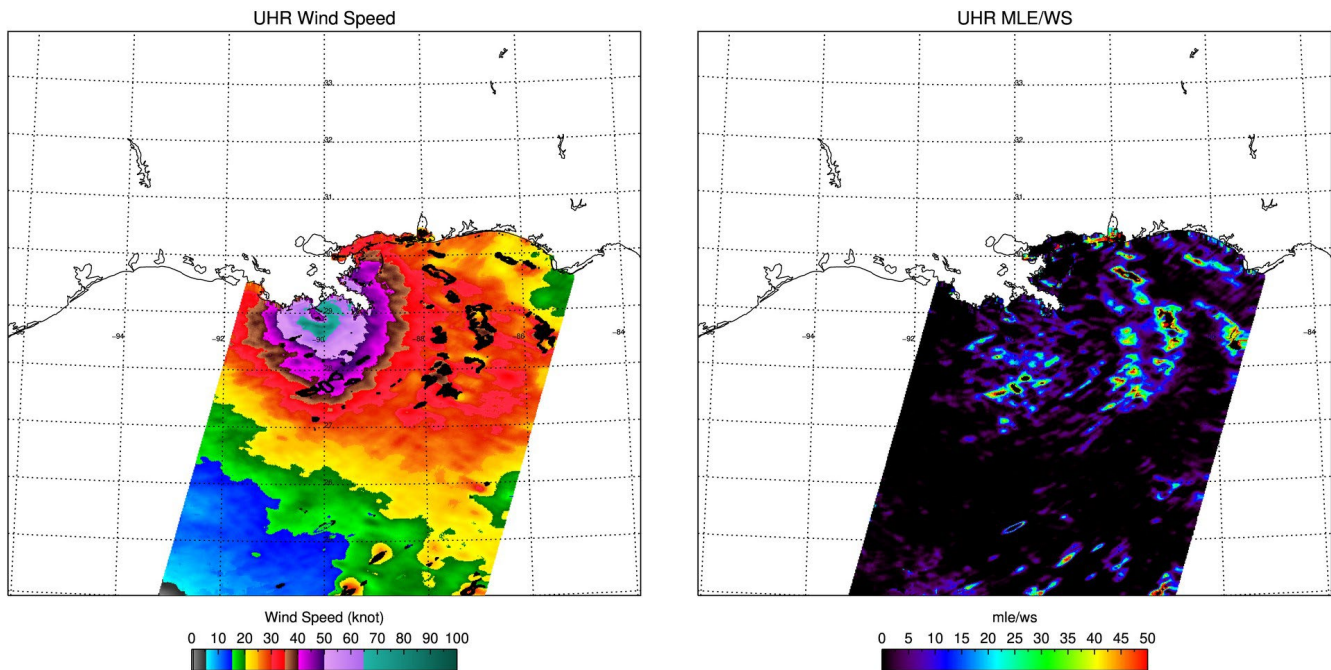

Fig. 9. (a) Hurricane Ida with rain flag. (b) The corresponding MLE_r.

VI. VALIDATION

The performance of the NOAA UHR ASCAT coastal processor was assessed by comparing wind retrievals with the 0.25-degree grid winds from the Global Data Assimilation System (GDAS), buoy winds from the National Data Buoy Center (NDBC) and the NOAA P-3 Stepped Frequency Microwave Radiometer (SFMR) winds. We focused the validation within 30 km of the coastal zone. For GDAS and buoy validations, we selected five coastal regions around the continental United States as shown in Fig. 10, where the collocation of ASCAT/GDAS and ASCAT/buoy was collected for 10 days of each month between October 2021 and September 2022 (120 days in total). The five coastal regions are selected for different coastal terrains: region 1 West coast of US where coastal wind is influenced by gap wind events from the California Coast Ranges and region 5 Alexander Archipelago characterized by many islands, regions 2 and 3 along the east coast of US and region 4 covering the Gulf of Mexico are characterized mainly by flat lands.
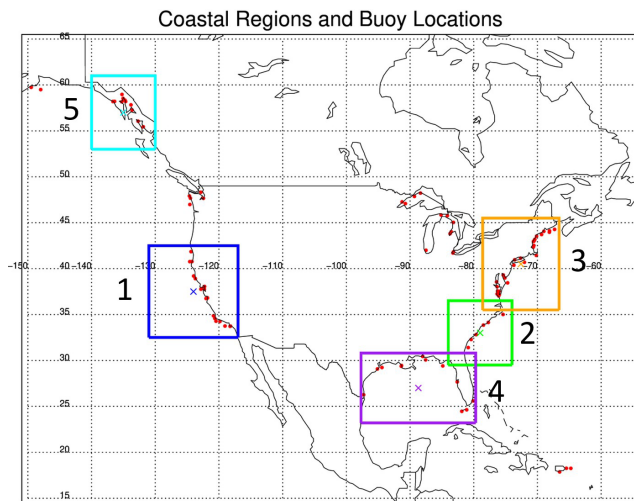

Fig. 10. Coastal regions used for UHR ASCAT coastal wind validation.

A. GDAS Comparison

In Fig. 11 we use the data shown in Fig. 6 to illustrate the assessment of retrievals within 30 km of the coast. In Fig 11 from top left panel clockwise are the UHR ASCAT coastal, GDAS, 12.5 km ASCAT and the uncorrected coastal wind speeds, respectively. The UHR ASCAT coastal wind speeds match the 12.5 km ASCAT winds where they are available before the land mask. The improvement from the land contamination in ASCAT coastal winds is evident when comparing to the uncorrected ASCAT coastal winds, where erroneous high winds around the coastline due to land contamination can be seen. From this example, the standard deviation of wind speeds with respect to GDAS is 1.8 m/s, 2.2 m/s and 3.1 m/s for 12.5 km ASCAT, UHR ASCAT coastal and

uncorrected UHR ASCAT coastal wind speeds, respectively. The performance of UHR ASCAT coastal winds are close to the 12.5 km winds but coverage now extends up to the coast.
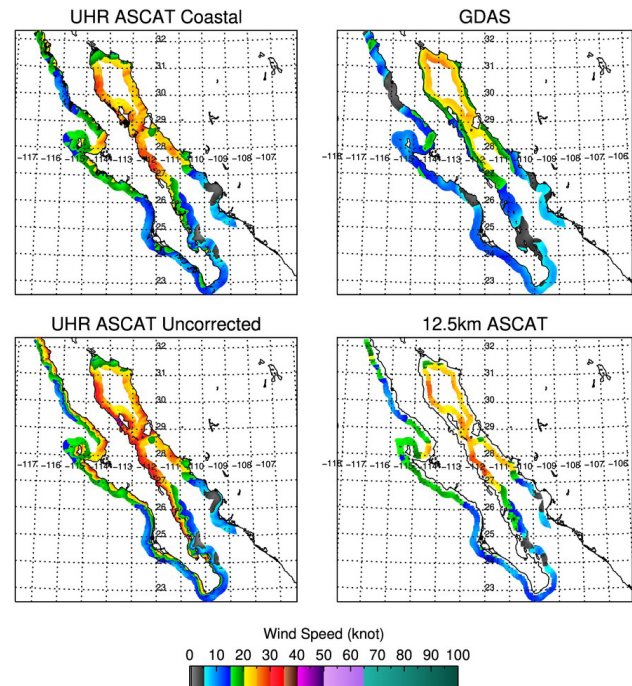

Fig. 11. Coastal wind speed within 30 km of the coast from different products.

It should be noted that although we have used the GDAS NWP as a reference in this comparison, it is widely known that NWP models often struggle to accurately capture local wind patterns, such as land-sea breezes, convective cells, and coastal orography-related wind variability. However, due to the lack of reliable sources and coverage for wind validation in coastal regions, the validation of performance with respect to GDAS should be considered as a statistical comparison. In an effort to improve the representativeness of GDAS in capturing true wind patterns, we have taken wind samples every 10 days of each month between October 2021 and September 2022 to better capture wind variability.

The UHR ASCAT coastal wind was tested using measurements over a 12-month period from the 5 regions depicted in Fig 10. The overall performance (within 30 km from the coast) with respect to GDAS wind speed and direction is shown in the density plots in Fig 12 (a) and (b), respectively. The total number of data points is approximately 6 million. The overall UHR wind speed has a bias of 1.4 m/s and a standard deviation of 2.3 m/s, which is slightly higher than the bias of 0.8 m/s and standard deviation of 1.7 m/s obtained by the conventional 12.5 km product. The UHR wind direction standard deviation is 38.6 degrees, compared to the 30.4 degrees obtained by the 12.5 km product. The reasons for the relatively larger wind direction standard deviation is a combination of a lack of the collocated 12.5 km wind direction

near the coast to support proper ambiguity removal, the increased measurement noise in the high-resolution product and the influence of direction uncertainty at the very low wind speeds.
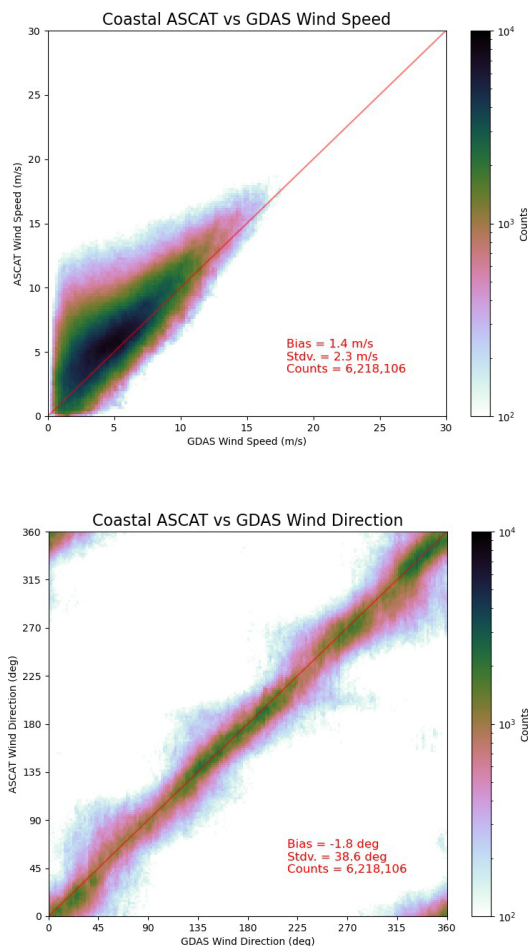

Fig. 12. (a) Coastal ASCAT wind speed vs GDAS's (b) Coastal ASCAT wind direction vs GDAS's.

The UHR ASCAT coastal wind is also evaluated as a function of distance from the coast. Fig. 13 shows the number of wind vector cells (WVC) of UHR ASCAT and 12.5-km winds as a function of distance within the 30 km coastal zone. As depicted in Fig 13, the majority of the 12.5 km wind retrievals are available up to ~20 km of the coast. After 20 km the number of available data points drops sharply. The availability of the UHR ASCAT wind retrievals is consistent throughout the 30 km coastal region. Fig 14 depicts the bias and standard deviation of the 12.5 km and UHR coastal winds as a function of distance from the coast. Until ~17 km of the coast both products perform identically. In the region between 1-17 km the error is systematically increasing. While the coastal winds error appears to be higher in that region due to a noisier nature of the high resolution, the mean wind speed is ~7.5 m/s almost the same as the 12.5km winds. It's also worth noting that there were only about 1,000 12.5km points compared to

100,000 UHR points. In Fig 15, we further evaluate the bias and standard deviation of the coastal wind product by aggregating the data into 0-2, 2-5, 5-10, 10-15 and > 15 m/s wind speed bins. As expected, the highest error, which is increasing with decreasing distance to the coast, is observed for winds lower than 5 m/s. The bias drops below 2 m/s for winds within 5-15 m/s already within 2 km of the coast. The bias of high wind retrievals >15m/s is ~10% of wind speed or lower for entire coastal region. The standard deviation drops below 2 m/s for all winds below 15 m/s at ~10 km from the coast. Slightly higher STD for winds above 15m/s is attributed to the fact that ASCAT CMOD5.H GMF was developed to provide better high wind performance while GDAS tends to have a negative bias for higher winds.

Finally, we evaluated the UHR ASCAT coastal wind relative to the geographical area of each region depicted in Fig. 10. The regional performance results are shown in Fig 16. The regions 2, 3 and 4 that are on the east coast of the US and Gulf of Mexico coastline are generally performing better than regions 1 and 5 from the US west coast and the Alaska. This behavior can be explained by the geographical location and impact of gap wind events from the mountain region as well as additional land contamination from Alexander Archipelago along Alaska coast. The correction of ocean sigma0 are more challenging in regions 1 and 5 due to the presence of mountainous terrain and small islands, in contrast to regions 2, 3, and 4 where the terrain is relatively flat.
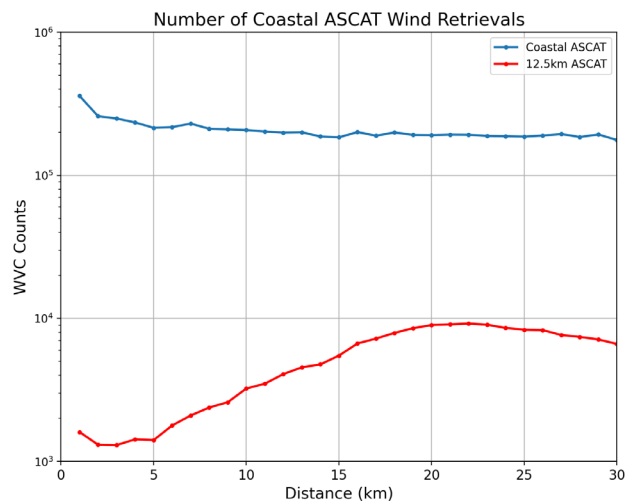

Fig. 13. Number of wind retrievals within 30km coastal zone from 5 regions for UHR coastal and 12.5 km ASCAT.
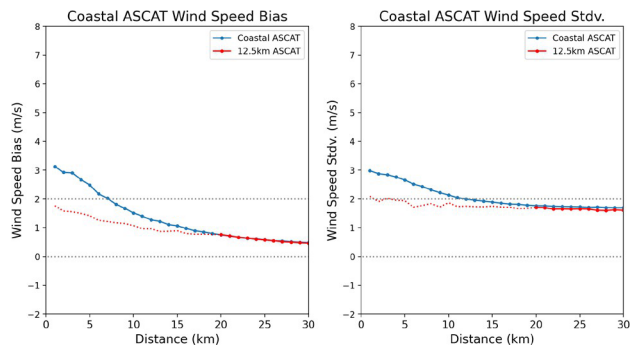
Fig. 14. Wind speed bias and standard deviation, with respect to GDAS NWP, as a function of distance from the coast.
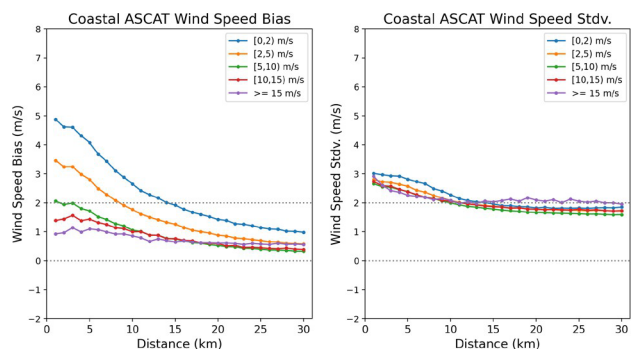

Fig. 15. Wind speed and bias standard deviation with respect to GDAS NWP as a function of distance for each wind speed group.
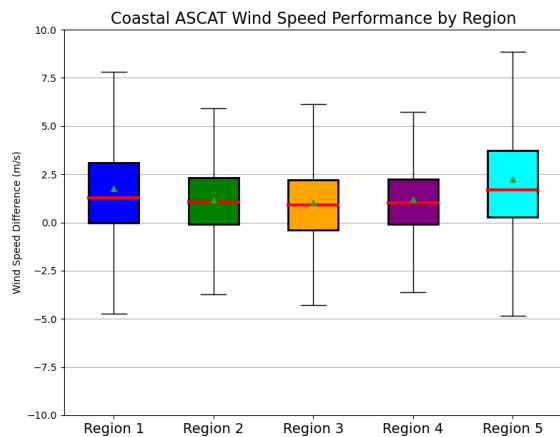

Fig. 16. A boxplot of wind speed performance for each region, with respect to GDAS NWP. The mean value is shown in the green triangles and the red lines represent the median.

B. Buoy Comparison

We evaluated the coastal winds with respect to NDBC buoy winds using the same 12-month period dataset as in the GDAS validation. The same data from the 5 regions within 30 km of the coast was matched up with buoys using the spatial and temporal criteria of 1-km and 1-hr, respectively. The spatial and temporal criteria were chosen to balance the impacts of wind variability while maximizing the number of data points available for statistical comparison. Since buoys observe wind with a higher temporal frequency than ASCAT, 1-hr time window results in multiple buoy measurements corresponding to the same ASCAT wind matchup. To address this issue, for each buoy we averaged all measurements corresponded to the same ASCAT observation before calculating any statistics. The buoy wind observations were adjusted to the equivalent 10-m height wind speed before being compare to the ASCAT winds [24]. The buoy locations are indicated by the red dots in Fig 10. After applying the quality control, there are a total of 14,482 wind comparisons collectively over 5 regions from 33 buoy stations. Fig. 17 shows a scatter plot of ASCAT coastal wind speed retrievals with respect to 1-hr averaged buoy wind speeds. The symbols are colored according to the buoy station ID and the symbol size is proportional to the distance from the coast, where the smallest size is closest to the coast. The overall ASCAT wind speed bias and standard deviation within 30 km of the coast are 0.6 m/s and 1.7 m/s, respectively. The number of buoys from each region are: 6, 4, 19, 3 and 1 for region 1-5, respectively. The ASCAT 12.5 km wind speed performance with respect to buoys as a function of coastal distance has a similar trend to Fig. 15 but quite noisy due to the small number of samples.
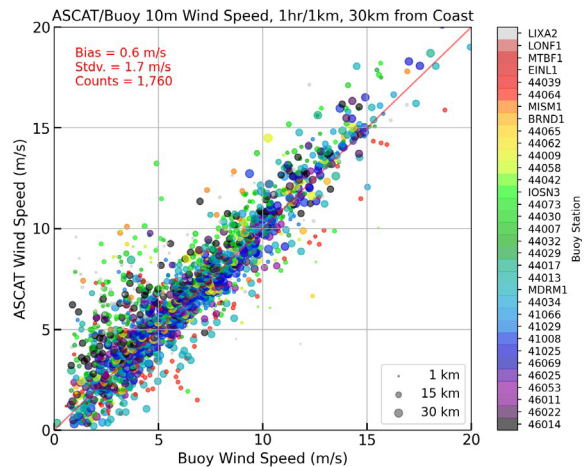

Fig. 17. Coastal ASCAT wind speed with respect to NDBC buoy wind speed.

C. SFMR Comparison

ASCAT coastal winds are also validated against those from the Stepped Frequency Microwave Radiometer (SFMR) aboard the NOAA Hurricane Hunter [25] utilizing data from a flight conducted in February 2, 2022 in the Bering sea coincident with the ASCAT-B pass shown in Fig. 18. The ASCAT-B pass and the SFMR track within a 1-hr window time is highlighted by dashed rectangular box along the Aleutian Islands. The SFMR processor does not produce winds closer than 2km of the coast

and those points are depicted by white dots on the track. Nevertheless, there was 903 data points of valid collocations between ASCAT and SFMR. The results of the comparison show the ASCAT wind speed has a bias of -1.4 m/s and a standard deviation of 1.7 m/s with respect to SFMR wind speeds and the scatter plot is presented in Fig. 19.
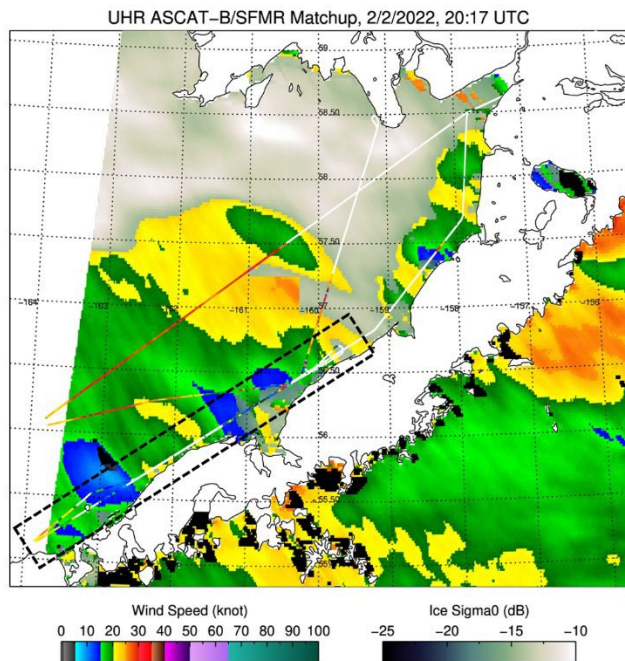

Fig. 18. ASCAT and SMFR collocation during the winter in February 2, 2022.
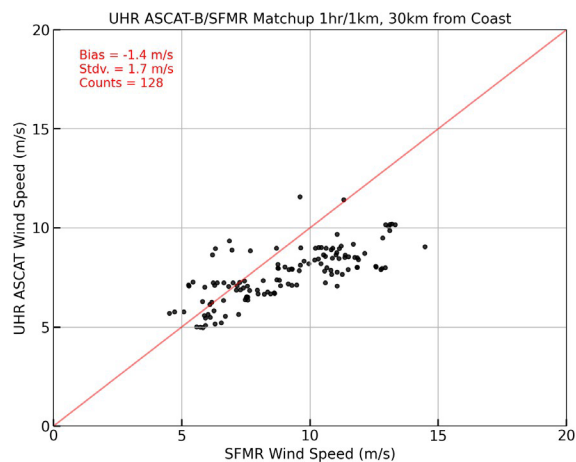

Fig. 19. Scatter plot of ASCAT and SMFR collocation corresponding to SMFR track in Fig. 18.

VII. CONCLUSION

In this paper, we present a high-resolution coastal wind data product from the near real-time ASCAT processing system. The motivation for this effort was to obtain wind retrievals in the data sparse coastal zone. The standard 12.5 and 25 km ASCAT wind vector cell grid size is too large to retrieve winds near the coast because of land contamination of the measurement. The combination of the finer spatial resolution and a novel technique we developed to correct land contamination of the normalized radar cross section in the coastal zone resulted in quality coastal wind retrievals. The coastal wind retrievals from ASCAT were evaluated within 30 km from the coast using a collocation dataset spanning a 12-month period using GDAS model winds and NDBC buoys from 5 selected coastal regions around the US. Additionally, the validation included a collocation with an SFMR NOAA P-3 flight on February 2, 2022. The UHR ASCAT coastal winds have a standard deviation of 2.3 m/s, 1.7 m/s and 1.7 m/s as compared to GDAS, buoy and SFMR winds, respectively. The comparison with buoy and SFMR winds show better performance than with GDAS, which is most likely because the spatial scales represented by the buoys and SFMR winds is more comparable to that of the ASCAT coastal wind product. The ASCAT coastal wind product performance exhibits a slightly larger standard deviation for winds within 10 km of the coast. However, for higher wind speeds the coastal wind biases and STD decrease nearly below 2 m/s. Finally, the coastal topography does appear to impact the performance statistics, where the coastal winds from the more mountainous regions of 1 and 5 show slightly higher standard deviation than region 2, 3 and 4.

REFERENCES

[1] J. Figa-Saldana, J. J. W. Wilson, E. Attema, R. Gelsthorpe, M. R. Drinkwater and A. Stoffelen, "The Advanced Scatterometer (ASCAT) on the Meteorological Operational (MetOp) platform: A follow on for European wind scatterometers," *Can. J. Remote Sens.,* vol. 28, no. 3, pp. 404-412, Jun. 2002.

[2] R. D. Lindsley, C. Anderson, J. Figa-Saldana and D. G. Long, "A Parameterized ASCAT Measurement Spatial Response Function," *IEEE Transactions on Geoscience and Remote Sensing,* vol. 54, no. 8, pp. 4570-4579, 2016.

[3] EUMETSAT, "ASCAT User Guide [EUM/OPS-EPS/MAN/04/0028]," Darmstadt, 2017.

[4] H. Hersbach, A. Stoffelen and S. Haan de, "An improved C0band scatterometer ocean geophysical model function: CMOD5," *J. Geophys. Res.,* vol. 112, no. C3, pp. C03006-1-C03006-18, Mar. 2007.

[5] A. Verhoef, M. Portabella, A. Stoffelen and H. Hersbach, "CMOD5.n - the CMOD5 GMF for neutral winds," OSI SAF report, SAF/OSI/CDOP/KNMI/TEC/TN/165, 2008.

[6] S. Soisuvarn, Z. Jelenak, P. S. Chang, S. O. Alsweiss and Q. Zhu, "CMOD5.H—A High Wind Geophysical Model Function for C-Band Vertically Polarized Satellite Scatterometer Measurements," *IEEE Transactions on Geoscience and Remote Sensing,* vol. 51, no. 6, pp. 3744-3760, 2013.

[7] A. Stoffelen, J. Verspeek, J. Vogelzang and A. Verhoef, "The CMOD7 Geophysical Model Function for ASCAT and ERS Wind Retrievals," *IEEE Journal of Selected Topics in Applied Earth Observations and Remote Sensing,* vol. 10, no. 5, pp. 2123-2134, 2017.

[8] P. S. Chang, Z. Jelenak, J. M. Sienkiewicz, R. Knabb, M. J. Brennan, D. G. Long and M. Freeberg, "Operational Use and Impact of Satellite Remotely Sensed Ocean Surface Vector Winds in the Marine Warning and Forecasting Environment," *Oceanography,* vol. 22, no. 2, pp. 194-207, 2009.

[9] D. S. Early and D. G. Long, "Image Reconstruction and Enhanced Resolution Imaging From Irregular Samples," *IEEE Trans. Geosci. Remote Sens.,* vol. 39, no. 2, pp. 291-302, 2001.

[10] D. G. Long, J. B. Luke and W. Plant, "Ultra high resolution wind retrieval from SeaWinds," in *IGARSS*, 2003.

[11] M. Spencer, C. Wu and D. G. Long, "Improved resolution backscatter measurements with the SeaWinds pencil-beam scatterometer," *IEEE Trans. Geosci. Remote Sens.,* vol. 38, no. 1, pp. 89-104, Jan. 2000.

[12] B. A. Williams, M. P. Owen and D. G. Long, "The ultra high resolution QuikSCAT product," in *IEEE Radar Conference*, 2009.

[13] R. D. Lindsley and D. G. Long, "Enhanced-Resolution Reconstruction of ASCAT Backscatter Measurements," *IEEE Transactions on Geoscience and Remote Sensing,* vol. 54, no. 5, pp. 2589-2601, 2016.

[14] S. Soisuvarn, Z. Jelenak, P. S. Chang and Q. Zhu, "Coastal Winds from NOAA Near Real-Time SCATSAT-1 Scatterometer Processor," in *OCEANS 2021 - MTS/IEEE*, San Diego-Porto, 2021.

[15] S. Soisuvarn, Z. Jelenak, P. S. Chang and Q. Zhu, "Coastal Winds and Sea Ice Detection from the NOAA Near Reat-Time Advanced Scatterometer (ASCAT) Processor," in *International Geoscience and Remote Sensing Symposium*, Kuala Lumpur, 2022.

[16] J. Verspeek, A. Stoffelen, A. Verhoef and M. Portabella, "Improved ASCAT Wind Retrieval Using NWP Ocean Calibration," *IEEE Transactions on Geoscience and Remote Sensing,* vol. 50, no. 7, pp. 2488-2494, 2012.

[17] J. Verspeek, A. Verhoef and A. Stoffelen, "ASCAT-B NWP Ocean Calibration and Validation," OSI SAF Technical Report, SAF/OSI/CDOP2/KNMI/TEC/RP/199, 2013.

[18] R. D. Lindsley, J. R. Blodgett and D. G. Long, "Analysis and Validation of High-Resolution Wind from ASCAT," *IEEE Transactions on Geoscience and Remote Sensing,* vol. 54, no. 10, pp. 5699-5711, 2016.

[19] M. P. Owen and D. G. Long, "Land Contamination Compensation for QuikSCAT Near-Coastal Wind Retrieval," *IEEE Transactions on Geoscience and Remote Sensing,* vol. 47, no. 3, pp. 839-850, 2009.

[20] F. M. Naderi, M. H. Freilich and D. G. Long, "Spaceborne radar measurement of wind velocity over the ocean-an overview of the NSCAT scatterometer system," *Proceedings of the IEEE,* vol. 79, no. 6, pp. 850-866, June 1991.

[21] D. W. Draper and D. G. Long, "An Assessment of SeaWinds on QuikSCAT Wind Retrieval," *Journal of Geophysical Research,* vol. 107, no. C12, pp. 3212-3226, Dec. 2002.

[22] A. Stoffelen and M. Portabella, "On Bayesian scatterometer wind inversion," *IEEE Transactions on Geoscience and Remote Sensing,* vol. 44, no. 6, pp. 1523-1533, June 2006.

[23] D. G. Long, P. Hardin and P. Whiting, "Resolution Enhancement of Spaceborne Scatterometer Data," *IEEE Trans. Geosci. Remote Sens.,* vol. 31, pp. 700-715, 1993.

[24] J. D. Holmes, Wind Loading of Structures, 3rd ed., Boca Raton, FL: CRC Press, 2015.

[25] J. W. Sapp, S. O. Alsweiss, Z. Jelenak, P. S. Chang and J. Carswell, "Stepped Frequency Microwave Radiometer Wind-Speed Retrieval Improvements," *Remote Sensing,* vol. 11, no. 3, p. 214, Jan. 2019.

Seubson Soisuvarn has an educational background in electrical engineering. He obtained his B.Eng. from Kasetsart University in Bangkok, Thailand in 1998, and later earned his M.S.E.E and Ph.D. from the University of Central Florida in 2001 and 2006 respectively. He has been a part of the NOAA Ocean Surface Winds Science Team since 2006 as a Project Scientist for the University Corporation for Atmospheric Research (UCAR) at the Center for Satellite Applications and Research under the National Environmental Satellite, Data, and Information Service (NESDIS) and the National Oceanic and Atmospheric Administration (NOAA). His areas of expertise include the development of algorithms for active and passive microwave remote sensing of ocean surface wind and the related new products.

Zorana Jelenak (Member, IEEE) received the Ph.D. degree in Physics from Waikato University, New Zealand, in 2000. Since 2001 Dr. Jelenak is a project scientist at UCAR and member of the Ocean Winds Team at NOAA/NESDIS/STAR. Her interests are in ocean remote sensing from active and passive microwave airborne and spaceborne instruments, with the emphasize on ocean wind and wave measurements. Of particular interest is data applicability in an operational near-real time environment, retrieval algorithm development, model function development, and advanced statistical analysis and error analysis for improved product and retrieval algorithm characterization.

Paul S. Chang (Senior Member, IEEE) received the Ph.D. Degree in electrical engineering in 1994 from the University of Massachusetts, Amherst. Since 1994, he has been a research physical scientist at the Center for Satellite Applications and Research, National Environmental Satellite, Data and Information Service (NESDIS), National Oceanic and Atmospheric Administration (NOAA). Current activities include research and development in active and passive microwave remote sensing of the ocean surface with an emphasis on retrieval of the ocean surface wind field. Wind retrieval algorithm improvements and new product developments are pursued through the analyses of satellite and aircraft microwave remote sensing data. An emphasis is placed on transitioning research results into operational use, which involves cooperative relationships with the operational facets of NESDIS and with the National Weather Service, a primary end user of this data.

1
2
3
4
5
6
7
8
9
10
11
12
13
14
15
16
17
18
19
20
21
22
23
24
25
26
27
28
29
30
31
32
33
34
35
36
37
38
39
40
41
42
43
44
45
46
47
48
49
50
51
52
53
54
55
56
57
58
59
60

Qi Zhu received the M.S. degree in information systems from Northeastern University, Boston, MA, in 2001. Since February 2002, she has been with the National Oceanic and Atmospheric Administration (NOAA) as a contractor, and she is currently a Senior Systems Analyst at Global Science and Technology, Inc. and member of the Ocean Winds Team at NOAA/NESDIS/STAR.
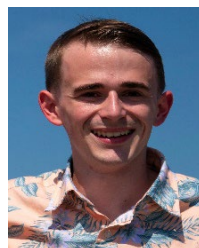
Casey G. Shoup received a B.S. degree in Meteorology, Atmospheric Science from the Pennsylvania State University, University Park in 2018, and a M.S. degree in Marine Science, Physical Oceanography from The University of South Carolina in 2020. He has been with the National Oceanic and Atmospheric Administration (NOAA) since graduating in 2020, serving as a Scientist with the Satellite Ocean Surface Winds group in STAR/NESDIS/NOAA, aiding with data acquisition, visualization, and product development.